POLYOXOMETALATES

Open Access
RESEARCH ARTICLE

Polyoxometalate-derived N@Mo_2C/V_2O_3 cluster heterostructure for accelerated alkaline hydrogen evolution reaction

Lulu Chen[1,2], Yichao Huang[1] ✉, Haitao Li[1], Ruili Gao[1], Han Tang[1], Jiangwei Chen[1], Yanfei Wang[1], Meihong Liao[3], and Chuande Wu[1]

[1] *State Key Laboratory of Chemical Safety, School of Materials Science and Engineering, China University of Petroleum (East China), Qingdao 266580, China*
[2] *School of Intelligent Manufacturing and Control Engineering, Shandong Institute of Petroleum and Chemical Technology, Dongying 257061, China*
[3] *School of Mechanical and Electronic Engineering, Qingdao Binhai University, Qingdao 266555, China*

Cite This: *Polyoxometalates*, **2026**, *5*, 9140110

Read Online

ABSTRACT: The hydrogen evolution reaction (HER) in alkaline water electrolysis is fundamentally limited by the high energy barrier associated with water dissociation. Herein, we report the development of self-supported nitrogen-doped molybdenum carbide and vanadium oxide cluster heterostructures (N@Mo_2C/V_2O_3) on carbon fiber paper using organoimido-derivatized molybdovanadate nanoclusters as precursors. Experimental results and theoretical calculations demonstrate that the engineered cluster heterointerfaces significantly reduce the energy barrier of the rate-determining step, accelerating HER kinetics. Moreover, V_2O_3 acts as a cocatalyst that enhances hydrophilicity of the N@Mo_2C/V_2O_3 and, versus pristine N@Mo_2C, facilitates hydrogen desorption from the composite. The optimized N@Mo_2C/V_2O_3 cluster heterostructure exhibits exceptional electrocatalytic performance, delivering a current density of 300 mA·cm^{-2} at an overpotential of merely 191 mV and maintaining stability over 400 h of continuous operation. When integrated into an alkaline water electrolyzer, the system requires only 1.94 V to achieve an industrially relevant current density of 500 mA·cm^{-2}, outperforming commercial platinum–carbon catalysts. These findings offer new perspectives and valuable insights into the development of efficient, stable, and economical noble metal-free electrocatalysts for green hydrogen production.

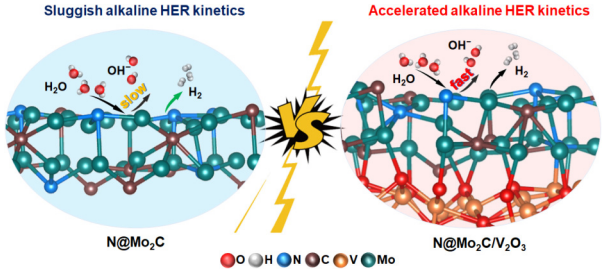

KEYWORDS: polyoxometalates, clusters, heterostructures, electrocatalysis, hydrogen evolution reaction

1 Introduction

Hydrogen production via water electrolysis, as a clean and sustainable energy-generation technology, holds profound significance in addressing the global energy crisis and alleviating environmental pollution [1]. By integrating electrolysis with renewable energy sources, abundant water resources can be effectively transformed into high-value hydrogen energy, thus providing steadfast support and a robust foundation for energy transition and eco-friendly green development [2, 3]. Compared with acidic water electrolysis, alkaline water electrolysis demonstrates distinct advantages, including lower cost, greater technological maturity, and superior electrode durability. However, despite these merits, the efficiency of hydrogen production in alkaline environments is significantly hindered by inherent complexity and sluggish kinetics associated with water adsorption and dissociation as well as the adsorption and desorption of reaction intermediate during the hydrogen evolution reaction (HER). These kinetic limitations not only reduce overall hydrogen production efficiency but also lead to substantial energy losses, presenting considerable challenges for practical applications [4]. Furthermore, under industrial operating conditions, namely high temperature (~ 80 °C), highly alkaline electrolyte (~ 30 wt.% KOH), and high current densities (> 300 mA·cm^{-2}), extensive gas bubbling is generated during alkaline water electrolysis to enhance hydrogen production efficiency. This vigorous gas evolution continuously stripps the catalyst surface, which places strict requirements on the stability of the electrode [5, 6]. These harsh conditions impose stringent requirements on electrode durability, prompting the development of self-supported catalysts that directly integrate active components into the electrode structure. Such designs not only enhance mechanical stability but also reduce manufacturing costs compared with conventional powder-based catalyst systems [7–10]. Moreover, the transition from laboratory-scale three-electrode configurations to industrial alkaline water electrolyzers presents

Received: September 24, 2025; **Revised:** December 23, 2025
Accepted: December 31, 2025

✉Address correspondence to yichaoh@upc.edu.cn

https://doi.org/10.26599/POM.2026.9140110

substantial challenges, particularly for powder catalysts that rely on polymeric binders. This well-defined aqueous electrolyte environment of a three-electrode cell fails to replicate the harsh conditions of zero-gap alkaline electrolyzers, which operates at elevated temperatures, high current densities, and under intense gas evolution. Consequently, the polymeric binders used to immobilize powder catalysts are prone to degradation, leading to catalyst detachment and rapid deactivation under these industrial operating conditions [6]. Consequently, there is an urgent need to develop integrated HER electrodes that combine high catalytic activity with long-term stability for practical industrial applications [11, 12].

The development of cost-effective electrocatalysts based on earth-abundant elements has become critically important owing to the high cost and limited availability of noble-metal, platinum-based materials [13]. Among the alternative candidates, molybdenum carbides (MoC and Mo_2C) have emerged as particularly promising HER catalysts, owing to their platinum-like electronic properties, high electrical conductivity, and exceptional electrochemical stability [14–16]. However, despite their advantages, pristine Mo_2C binds hydrogen quite strongly because of the high density of the empty Mo d orbitals, which hinders the desorption of active hydrogen [17]. Tuning the electronic structure of Mo_2C through heteroatom incorporation can effectively improve its hydrogen adsorption energy and enhance HER catalytic performance [18–20]. Nevertheless, in alkaline media, HER kinetics involve additional critical steps beyond hydrogen adsorption, including water molecule adsorption and activation as well as hydroxyl intermediate (OH^-) desorption, which together can govern the overall reaction rate [21–23]. Single-component catalysts typically fail to simultaneously satisfy all these kinetic requirements, often resulting in suboptimal catalytic performance [24]. Therefore, the integration of two or more catalytic materials to form heterostructures has emerged as a highly effective strategy for boosting catalyst activity.

Recent studies have demonstrated that the high electronegativity of V_2O_3 can effectively destabilize surface-adsorbed water molecules, thereby enhancing water polarization and significantly accelerating water dissociation kinetics [25, 26]. Moreover, V_2O_3 exhibits extremely weak hydrogen binding energy [25], which can promote efficient hydrogen desorption at heterointerfaces. In this context, constructing heteroatom-doped Mo_2C/V_2O_3 heterojunctions in self-supported architectures may provide an effective strategy to overcome kinetic limitations in alkaline HER systems. Polyoxometalates (POMs), a class of anionic clusters comprising early transition metals (Mo, V, and W) and oxygen [27], offer unique advantages for catalyst design [28–30], including atomic-level structural precision and uniform sizes (~ 1 nm) [31–37]. In particular, POMs are well suited as precursors for constructing molybdenum carbide-based heterojunctions [19, 38]. POMs enable not only the targeted incorporation of heteroatoms through organic functionalization but also the precise engineering of POM frameworks containing specific metallic heteroatoms, making them exceptionally versatile building blocks for advanced catalyst development [15, 18, 39, 40].

Heterostructured catalysts, including metal–carbide [41], carbide–oxide [42], nitride–carbide [43, 44], nitride–oxide [26, 45] systems, among others [46], have emerged as powerful platforms for tuning interfacial electronic structures. Lattice mismatch and work-function differences across heterointerfaces create built-in electric fields and charge redistribution regions [24], which modulate the adsorption energies of key intermediates and accelerate electron transfer. Particularly, oxide–nitride heterostructures integrate the strong water activation capability of oxides with the high conductivity and favorable hydrogen adsorption of carbides [26], thereby enabling balanced Volmer–Heyrovsky kinetics in the alkaline HER [45]. Consequently, the rational design of such electronically coupled heterointerfaces represents an effective strategy to overcoming the intrinsic limitations of single-phase catalysts and achieving superior catalytic efficiency.

Inspired by these studies, we synthesized a Mo–V POM precursor consisting of a polyarylimido-stabilized molybdovanadate cluster ($[V_4Mo_3O_{14}(NAr)_3(l2\text{-}NAr)_3]^{2-}$], denoted as Mo3V4-NAr) [33]. Subsequent one-step pyrolysis of this precursor yielded $N@Mo_2C/V_2O_3$ cluster heterostructures featuring abundant heterogeneous interfaces.

This innovative approach successfully addresses two fundamental challenges in heterostructure fabrication: precise control over interfacial formation and the limited interfacial contact areas typically observed in conventional systems. By leveraging the well-defined molecular architecture of the Mo3V4-NAr POM precursors stabilized by arylimido ligands, nanocrystal growth was effectively confined during pyrolysis, resulting in the formation of uniform $N@Mo_2C/V_2O_3$ cluster heterostructures. The resulting heterostructured architecture not only effectively enhances surface hydrophilicity and accelerates reaction kinetics but also optimally modulates the electronic structure and interfacial charge distribution of the $N@Mo_2C/V_2O_3$ cluster heterostructure. These synergistic effects can effectively reduce the energy barrier of the rate-determining step and optimize the binding energies of key HER intermediates (OH^- and H^*). Consequently, the optimized $N@Mo_2C/V_2O_3$ cluster heterostructure exhibits remarkable catalytic activity and robust high-current stability under alkaline conditions for the HER, achieving a current density of 300 $mA{\cdot}cm^{-2}$ at an overpotential of just 191 mV and maintaining stable operation for over 400 h, significantly outperforming conventional 20 wt.% Pt/C catalysts. Moreover, when implemented in an alkaline water electrolyzer (AWE), this catalyst requires only 1.94 V to drive a current density of 500 $mA{\cdot}cm^{-2}$, demonstrating its immense potential for practical and industrial applications.

2 Method

2.1 Preparation of $N@Mo_2C/V_2O_3$

Carbon fiber paper (CFP) was first subjected to ultrasonic cleaning in deionized water, ethanol, and acetone, followed by drying in an oven. The Mo3V4-6NAr POM precursor was subsequently redissolved in acetonitrile and homogenized via ultrasonication to obtain a homogeneous solution. This solution was drop-cast onto the precleaned CFP to ensure complete infiltration. After drying, the CFP was uniformly coated with *in situ*-grown POMs. Subsequently, the coated CFP was transferred to a tubular furnace for thermal treatment at 650 °C for 3 h under a reducing atmosphere (8% H_2/Ar), yielding the $N@Mo_2C/V_2O_3$ cluster heterostructure. To investigate the influence of calcination temperature on phase composition and alkaline HER electrocatalytic performance, additional comparative samples were synthesized using identical procedures at varying temperatures (600, 700, 800, and 900 °C).

2.2 Preparation of N@Mo_2C and V_2O_3

For comparison, N@Mo_2C and V_2O_3 catalysts were synthesized separately using $[(C_4H_9)_4N]_2[Mo_6O_{13}(NC_6H_5)_6]$ (denoted as Mo6-6NAr) and $[(C_4H_9)_4N]_3[H_3V_{10}O_{28}]$ (abbreviated as V10) as precursors, respectively. Except for the use of different precursors, all synthesis procedures were identical to those used for the N@Mo_2C/V_2O_3 composite, ensuring consistency across all prepared samples.

2.3 Electrochemical measurements

The HER performance of commercial 20 wt.% Pt/C, N@Mo_2C/V_2O_3, N@Mo_2C, and V_2O_3 catalysts was evaluated using a standard three-electrode system at room temperature with a CHI760E electrochemical workstation. For the Pt/C benchmark catalyst, a homogeneous catalyst ink was prepared by dispersing 5.0 mg of 20 wt.% Pt/C in 950 μL of a water/isopropanol mixture (1:1 v/v), followed by the addition of 50 μL of 5 wt.% Nafion solution. The resulting mixture was ultrasonicated for 30 min to ensure uniform dispersion. Subsequently, 100 μL of the catalyst ink was drop-cast onto a 1 cm × 1 cm carbon paper substrate. After drying, the working electrode was obtained with a Pt/C loading of 0.5 mg·cm^{-2}. A carbon rod and a reversible hydrogen electrode (RHE) were used as the counter and reference electrodes, respectively. Linear sweep voltammetry was performed over a potential window of −0.5 to 0.05 V (vs. RHE) at a scan rate of 5 mV·s^{-1}, with 95% *iR* compensation applied. Tafel slopes were determined by linear fitting of the corresponding polarization curves. The electrochemical double-layer capacitance (C_{dl}) was determined from cyclic voltammetry (CV) measurements conducted in a non-Faradaic potential range (0.1–0.3 V vs. RHE) at varying scan rates (10–60 mV·s^{-1}). Additionally, electrochemical impedance spectroscopy (EIS) was performed at open-circuit potential over a frequency range of 0.01–100,000 Hz.

2.4 Solar-driven water electrolysis cell testing

The system was constructed by connecting commercial solar panels (12 V, 12 W output under standard illumination) to a two-electrode setup. Hydrogen gas produced by the integrated system under natural sunlight irradiation was collected using the water displacement method.

2.5 Alkaline water electrolyzer testing

An AWE was configured in a two-electrode setup for evaluating the electrolysis efficiency of the catalysts. The cathode was a self-supporting N@Mo_2C/V_2O_3 electrode with a large geometric area of 12.56 cm^2 (radius = 2 cm), along with a commercial Zirfon separator. The anode consisted of either commercial Raney nickel (purchased from Anhui Weishui New Energy Technology Co., Ltd.) or a NiFe layered double hydroxide (NiFe‐LDH) catalyst [47] for comparative assessment. The electrolyte was a 30% KOH solution, and all electrochemical measurements were performed at 60 °C under atmospheric pressure. Polarization curves were recorded from open-circuit voltage to high current densities, while galvanostatic stability tests were conducted at a constant current density of 500 mA·cm^{-2} to evaluate long-term stability of the as-prepared catalysts. All assembly tests were repeated three times, and the results were averaged for accuracy. To further assess the performance of the AWE, additional tests were conducted at varying temperatures (20, 40, and 60 °C).

3 Results and discussion

3.1 Synthesis of electrocatalysts

The synthetic route for the N@Mo_2C/V_2O_3 cluster heterostructure is schematically illustrated in Scheme 1, with detailed procedures provided in the Methods section. Initially, a well-defined Mo3V4-6NAr POM precursor was synthesized (Fig. S1 in the Electronic Supplementary Material (ESM)), comprising six arylimido ligands covalently functionalized on the organometallic POM framework. This precisely engineered precursor features an atomic Mo:V ratio of 3:4 within each molecule. Concurrently, the strategic

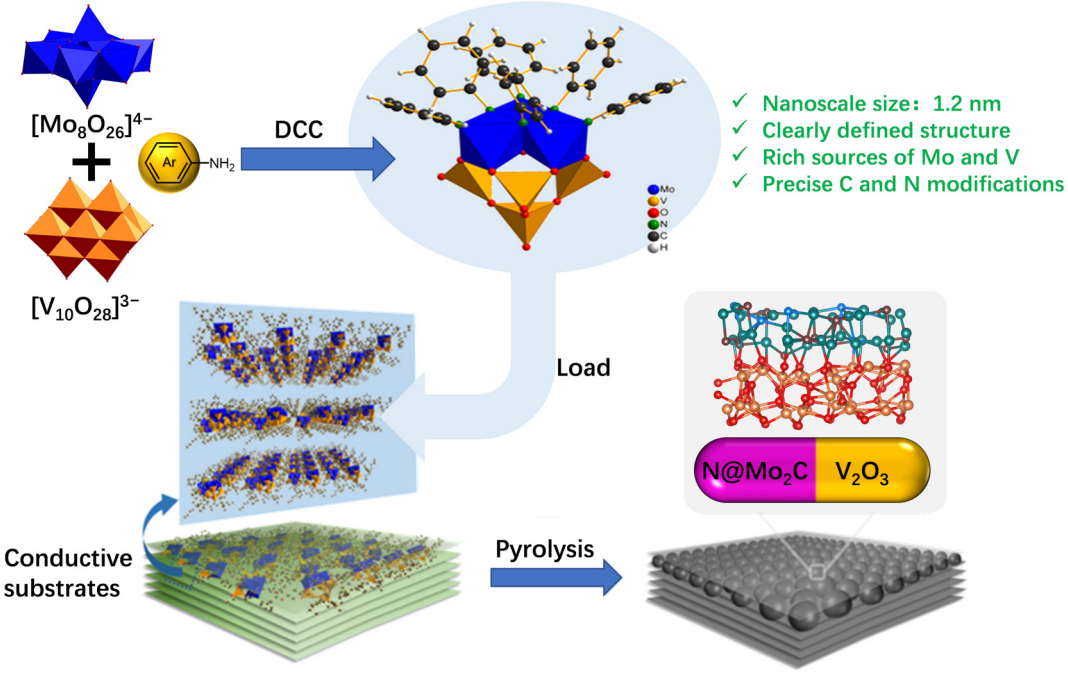

Scheme 1 Schematic illustration of the synthesis of N@Mo_2C/V_2O_3.

incorporation of Mo–N bonds via the arylimido ligands enables controllable nitrogen doping into Mo_2C [15], allowing for atomic-level nitrogen doping in Mo_2C.

3.2 Morphological and structural characterizations

The scanning electron microscopy (SEM) image in Fig. S2(a) in the ESM displays the morphology of the pristine CFPs, with individual carbon fibers exhibiting a diameter of ~ 8 μm. The fiber surfaces exhibit a rough texture with distinct longitudinal striations, which can facilitate the heterogeneous nucleation and recrystallization of POM molecules. Figures S2(b)–S2(d) in the ESM illustrate the morphologies of Mo3V4-6NAr, Mo6-6NAr, and V10 grown on the carbon fibers. SEM images clearly demonstrate that the POM molecules form a homogeneous conformal coating on the fiber surfaces, completely encapsulating the substrates. This uniform coating ensures robust interfacial adhesion between the POM molecules with the conductive carbon paper during subsequent thermal processing. The POM-loaded carbon paper was subsequently pyrolyzed, and the resulting products were subjected to comprehensive phase composition analysis and microstructural characterization. The X-ray diffraction (XRD) patterns shown in Fig. 1(a) demonstrates that the pyrolysis product of Mo6-6NAr exhibits diffraction peaks consistent with the standard reference pattern PDF#72-1683 for molybdenum carbide (Mo_2C). This confirms the successful formation of phase-pure Mo_2C through pyrolysis. By contrast, the V10-derived product exclusively matches the vanadium(III) oxide reference (PDF#71-0343), verifying the formation of V_2O_3. The XRD pattern of the Mo3V4-6NAr pyrolysis product exhibits well-defined diffraction peaks corresponding to both Mo_2C and vanadium oxide (V_2O_3), unambiguously demonstrating the formation of a $N@Mo_2C/V_2O_3$ cluster heterostructure. Notably, the diffraction peaks of $N@Mo_2C/V_2O_3$ are broader than those of the individual $N@Mo_2C$ and V_2O_3. This peak broadening suggests mutual inhibition of crystalline growth between these two heterostructured components (Fig. S3 and Table S2 in the ESM), effectively suppressing nanoparticle aggregation and Ostwald ripening [32, 48].

As shown in Fig. S3 in the ESM, $N@Mo_2C/V_2O_3$, $N@Mo_2C$, and V_2O_3 were uniformly deposited on carbon fibers, forming a robust catalyst layer strongly adhered to the carbon paper substrate. This intimate contact facilitates efficient electron transfer between the active materials and the conductive carbon paper. High-magnification imaging (Fig. 1(b) and Fig. S3(d) in the ESM) revealed that the $N@Mo_2C/V_2O_3$ surface consists of abundant nanosheets with pronounced protrusions. By contrast, $N@Mo_2C$ exhibits a smoother morphology with densely packed nanoparticle

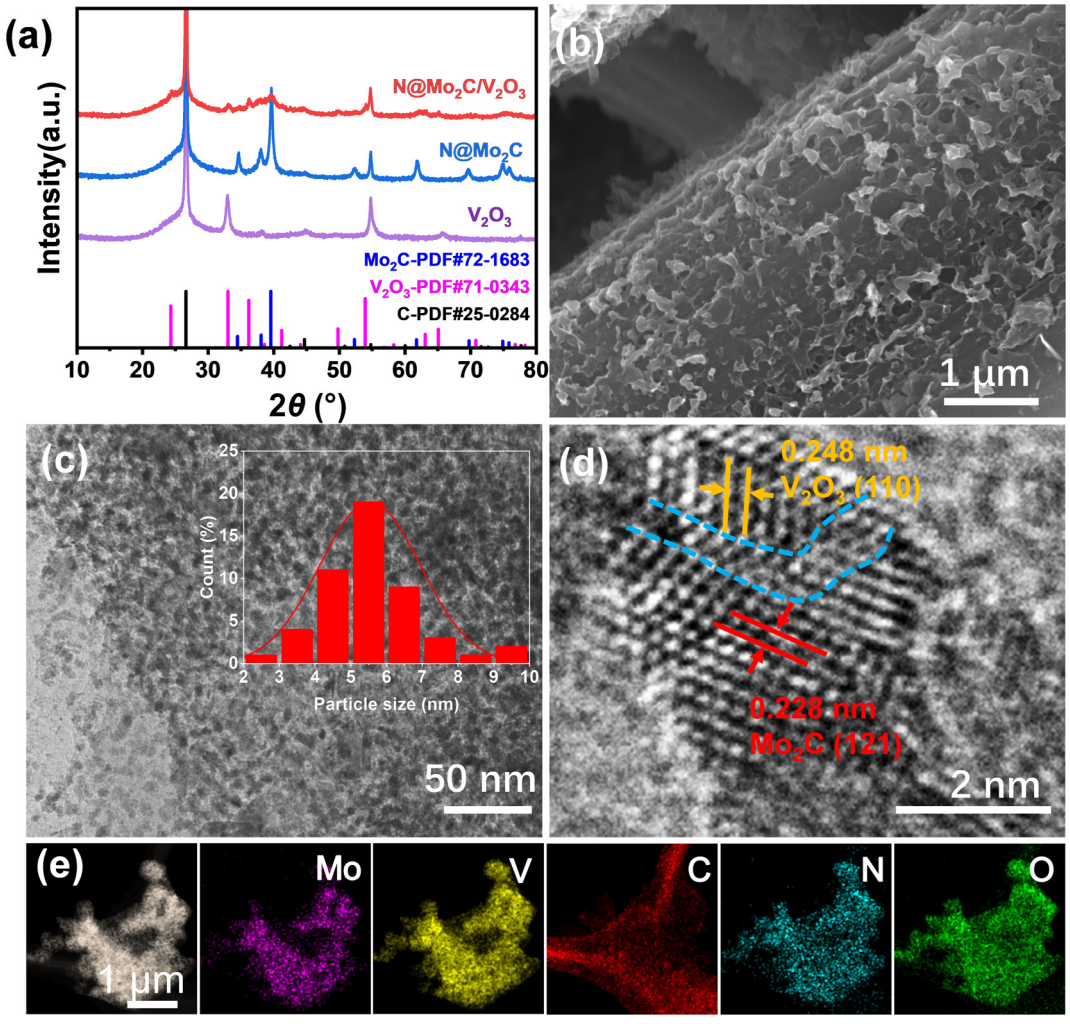

Figure 1 (a) XRD patterns of $N@Mo_2C/V_2O_3$, $N@Mo_2C$, and V_2O_3. (b) SEM image of $N@Mo_2C/V_2O_3$. (c) TEM image and nanoparticle size distribution histogram (insert) of $N@Mo_2C/V_2O_3$. (d) HRTEM image of $N@Mo_2C/V_2O_3$. The blue dashed line(s) in the figure represent the heterointerface between $N@Mo_2C$ and V_2O_3. (e) EDX elemental mappings of $N@Mo_2C/V_2O_3$.

(Fig. S3(e) in the ESM), whereas V_2O_3 displays larger, well-defined nanosheets with a porous structure (Fig. S3(f) in the ESM). Notably, the nanosheets in N@Mo_2C/V_2O_3 are significantly finer than those observed in pristine V_2O_3. Moreover, transmission electron microscopy (TEM) reveals distinct structural differences among the catalysts. The V_2O_3 catalyst consists of nanoparticles with diameters of 20–30 nm (Fig. S3(i) in the ESM), whereas the N@Mo_2C catalyst consists of smaller nanoparticles (~ 10 nm, Fig. S3(h) in the ESM). By contrast, the N@Mo_2C/V_2O_3 cluster heterostructure exhibits a highly dispersed nanosheet morphology with ultrafine nanoparticles of only 5–6 nm (Fig. 1(c) and Fig. S3(g) in the ESM). These observations suggest that the existence of V_2O_3 modifies the structural evolution of N@Mo_2C on the carbon paper substrate, resulting in a heterojunction catalyst with significantly reduced particle size and an open, porous architecture. The catalysts were further characterized for their specific surface area and pore structure using the Brunauer–Emmett–Teller (BET) and Barrett–Joyner–Hallender methods [33, 49], respectively. The N@Mo_2C/V_2O_3 cluster heterostructure exhibited a high BET surface area of 79.326 $m^2 \cdot g^{-1}$ with an average pore size of 3.43 nm (Fig. S4 in the ESM). Raman spectroscopy (Fig. S5 in the ESM) suggests that the incorporated amorphous carbon likely inhibits N@Mo_2C/V_2O_3 nanoparticle growth while stabilizing the nanosheet morphology of N@Mo_2C/V_2O_3 [15].

Furthermore, a representative high-resolution TEM (HRTEM) image is shown in Fig. 1(d), clearly revealing well-defined lattice fringes with interplanar spacings of 0.228 and 0.248 nm, which correspond to the (121) plane of Mo_2C and the (110) plane of V_2O_3, respectively. A distinct heterojunction interface forms between these two crystallographic planes, as marked by the blue dashed line in Fig. 1(d). Energy-dispersive X-ray spectroscopy (EDX) elemental mapping further demonstrates the uniform distribution of Mo, V, C, N, and O throughout the N@Mo_2C/V_2O_3 composite, with no observable agglomeration (Fig. 1(e)). By combining EDX data with the inductively coupled plasma atomic emission spectrometry results (Table S1 in the ESM), the atomic mass fractions of Mo, V, and N in N@Mo_2C/V_2O_3 were determined to be 17.07%, 10.31%, and 6.24%, respectively. Interestingly, the derived atomic ratios of Mo:V (1:1.14) and Mo:N (1:2.42) closely match those of the initial Mo3V4-6NAr precursor (Mo:V = 1:1.33, Mo:N = 1:2), indicating that the Mo, V, and N heteroatoms in the POM molecular precursor are well retained in the final catalyst, ultimately forming a cluster heterojunction. For the N@Mo_2C/V_2O_3 cluster heterostructure, the carbon content was excluded from the quantitative analysis owing to its excessive contribution from the carbon fiber substrate following ultrasonic detachment and mechanical grinding.

To elucidate the chemical composition and valence states of the N@Mo_2C/V_2O_3 cluster heterostructure, X-ray photoelectron spectroscopy (XPS) was employed. As shown in Fig. 2(a), the XPS survey spectrum confirms the presence of Mo, V, C, N, and O as the primary elements of the N@Mo_2C/V_2O_3 cluster heterostructure. The high-resolution Mo 3d spectrum (Fig. 2(b)) reveals three distinct doublets corresponding to different molybdenum oxidation states. The binding energies observed at 228.5 and 231.5 eV are assigned to the $3d_{5/2}$ and $3d_{3/2}$ orbitals of Mo^{2+} in Mo_2C [8, 15], respectively. Peaks at 229.4 and 233.5 eV correspond to the $3d_{5/2}$ and $3d_{3/2}$ orbitals of Mo^{4+} in MoO_2 [18], whereas those at 232.6 and 235.8 eV are attributable to Mo^{6+} in MoO_3, likely arising from surface oxidation of the molybdenum species in the N@Mo_2C/V_2O_3 [8, 18, 50, 51]. Notably, compared to N@Mo_2C, the Mo^{2+} and Mo^{4+} peaks in N@Mo_2C/V_2O_3 exhibit reduced intensity, whereas the Mo^{6+} peak becomes more pronounced and shows a slight positive shift (~ 0.15 eV) in binding energy. This observation suggests that the incorporation of V_2O_3 induces interfacial charge redistribution in N@Mo_2C/V_2O_3, leading to electron depletion from Mo and a consequent increase in its oxidation state. Charge transfer at the heterojunction interface is also expected to influence the valence states of neighboring V species. As illustrated in Fig. 2(c), the V 2p spectrum reveals that the binding energies of V^{3+} (515.22 and 522.74 eV), V^{4+} (516.50 and 524.11 eV), and V^{5+} (517.53 and 525.22 eV) in N@Mo_2C/V_2O_3 are slightly lower (~ 0.1 eV) than those in pristine V_2O_3 [26, 52, 53]. This shift implies strong interfacial charge transfer between the two components in the N@Mo_2C/V_2O_3 cluster heterostructure, which may enhance the activation of catalytic sites.

Additionally, the C 1s spectrum (Fig. 2(d)) exhibits multiple fitted peaks, where the minor shoulder at 283.26 eV corresponds to the C–Mo bond in Mo_2C [15]. The dominant peak at 284.8 eV is assigned to graphitic carbon (C–C), whereas the signal at 286.31 eV arises from nitrogen-doped carbon (C–N) [54, 55]. A weak peak at 288.23 eV is attributable to C–O bonding. Figure 2(e) shows the high-resolution N 1s spectrum, confirming the presence of Mo 3p (395.03 eV), Mo–N (397.50 eV), pyridinic-N (398.82 eV), pyrrolic-N (400.40 eV), and graphitic-N (401.40 eV) [50, 51]. The detection of Mo–N bonds in N@Mo_2C/V_2O_3 confirms the successful incorporation of nitrogen into the Mo_2C lattice. Moreover, previous studies indicate that pyrrolic nitrogen acts as an active site for the HER and effectively improves the electrical conductivity of the carbon substrate [56]. In the O 1s spectrum (Fig. 2(f)), the fitted peaks at 533.10, 532.03, and 530.73 eV are assigned to adsorbed water molecules, O–C, and O–Mo bonds [50], respectively.

3.3 Electrochemical performance

The electrocatalytic HER performance of the N@Mo_2C/V_2O_3 cluster heterostructure was evaluated using a standard three-electrode system in 1.0 M KOH alkaline electrolyte. To optimize the activity of cluster heterostructure catalysts, the effects of precursor loading and pyrolysis temperature on their phase composition and HER performance were systematically examined (Figs. S6 and S7 in the ESM). Optimal HER performance was achieved with a precursor loading of 10 μmol and a pyrolysis temperature of 650 °C, conditions under which well-defined coexisting Mo_2C and V_2O_3 phases were formed. For comparative analysis, control samples of N@Mo_2C and V_2O_3 were synthesized and tested under identical conditions.

XRD analysis (Fig. S8 in the ESM) reveals that the incorporation of V_2O_3 in the N@Mo_2C/V_2O_3 cluster heterostructure effectively suppresses particle agglomeration compared to single-phase N@Mo_2C derived from Mo6-6NAr, leading to enhanced HER activity. To ensure rigorous performance benchmarking, commercially available 20 wt.% Pt/C was used as a reference catalyst. As shown in Fig. 3(a), the Pt/C catalyst exhibits a low overpotential of 20 mV to achieve a current density (j) of 10 $mA \cdot cm^{-2}$, whereas the N@Mo_2C/V_2O_3 cluster heterostructure requires a higher overpotential of ~ 67 mV. However, at overpotentials (η) exceeding 160 mV, the cathodic current of the N@Mo_2C/V_2O_3 cluster heterostructure increases sharply, eventually surpassing that of the Pt/C catalyst. This enhanced performance suggests that the integrated heterojunction catalyst, directly grown

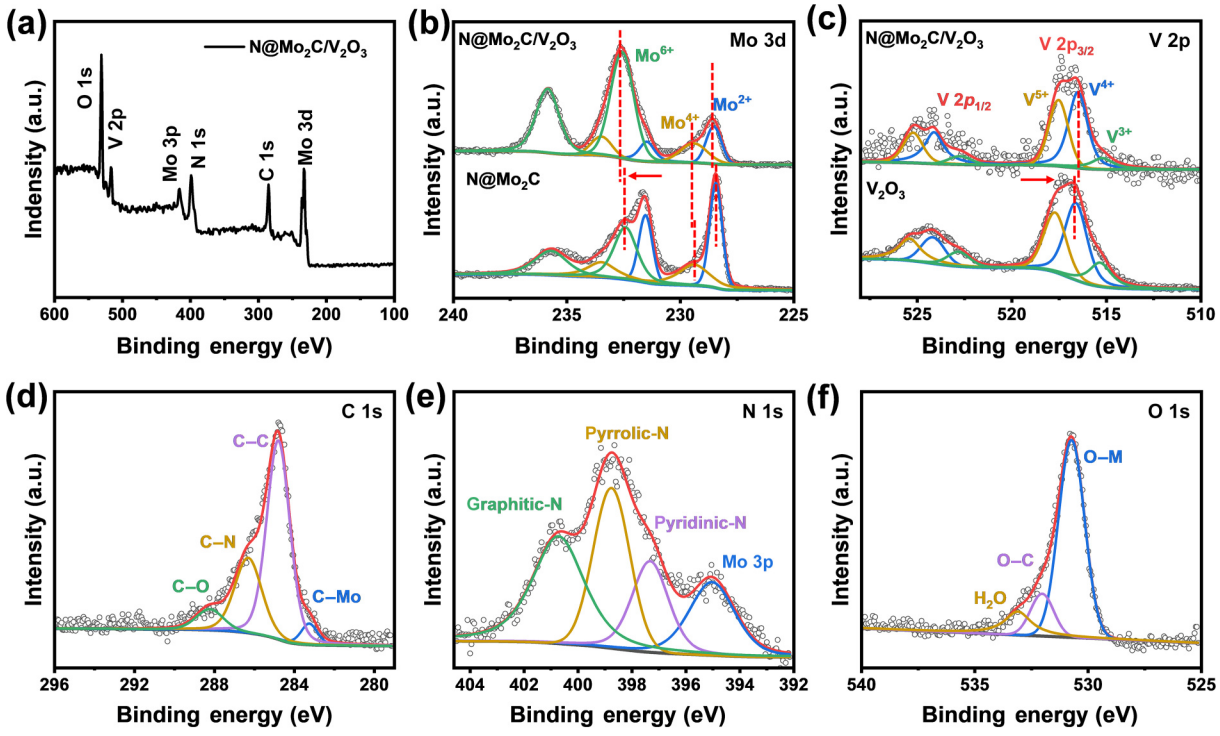

Figure 2 XPS analysis of $N@Mo_2C/V_2O_3$. (a) XPS survey spectrum of $N@Mo_2C/V_2O_3$. (b)–(f) High-resolution XPS signals of (b) Mo 3d; (c) V 2p; (d) C 1s; (e) N 1s; (f) O 1s.

on carbon paper, facilitates superior reaction kinetics by promoting efficient mass and charge transfer during the electrochemical process. Furthermore, the Tafel slope of $N@Mo_2C/V_2O_3$ at low current density was determined to be 64 mV·dec^{-1} (Fig. 3(b)), higher than that of commercial Pt/C (38 mV·dec^{-1}) but significantly lower than those of pristine $N@Mo_2C$ and V_2O_3 (75 and 317 mV·dec^{-1}, respectively). This indicates that the HER on the $N@Mo_2C/V_2O_3$ cluster heterostructure proceeds via the Volmer–Heyrovsky mechanism. Notably, $N@Mo_2C/V_2O_3$ achieves an impressive current density of 300 mA·cm^{-2} at a low overpotential of just 191 mV (Fig. 3(c)), outperforming commercial Pt/C (239 mV) and most previously reported non-noble metal catalysts. Combined with its cost-effectiveness and high efficiency, the $N@Mo_2C/V_2O_3$ cluster heterostructure exhibits exceptional HER performance under high-current conditions, demonstrating its significant potential for commercial electrolyzer applications.

The C_{dl}, determined through CV measurements in the non-Faraday potential region at various scan rates (Fig. S9 in the ESM), serves as a reliable indicator of the electrochemically active surface area (ECSA) [57]. As shown in Fig. 3(d), the $N@Mo_2C/V_2O_3$ cluster heterostructure exhibits a remarkably high C_{dl} of 137 mF·cm^{-2}, substantially surpassing those of its individual components (120 mF·cm^{-2} for $N@Mo_2C$ and 52 mF·cm^{-2} for V_2O_3). These results clearly demonstrate that the dual-component $N@Mo_2C/V_2O_3$ cluster heterostructure provides abundant active sites, which directly correlates with its superior HER performance. EIS is commonly employed to investigate charge transfer kinetics in electrocatalytic systems [34, 58]. As shown in Fig. S10 and Table S3 in the ESM, the $N@Mo_2C/V_2O_3$ cluster heterostructure exhibits a significantly lower charge transfer resistance (1.99 Ω) compared to its individual components ($N@Mo_2C$ and V_2O_3), reflecting its superior charge transfer efficiency and enhanced HER kinetics [59]. Further EIS measurements were performed on $N@Mo_2C/V_2O_3$ at different applied potentials, as illustrated in the Nyquist and Bode plots (Figs. S10(c) and S10(d) in the ESM). The impedance spectra reveal consistent electrochemical behavior across various overpotentials, indicating stable reaction kinetics throughout the HER process. In addition, the charge transfer resistance decreases progressively with increasing potential, confirming that the $N@Mo_2C/V_2O_3$ cluster heterostructure can maintain excellent HER performance even under high-current density conditions [34].

The electrochemical stability of the $N@Mo_2C/V_2O_3$ cluster heterostructure was evaluated over 3,000 consecutive CV cycles. As illustrated in Fig. 3(e), the polarization curves before and after cycling are nearly identical, with no observable potential shift. Furthermore, post-stability characterization confirmed that the phase structure and chemical composition of the $N@Mo_2C/V_2O_3$ cluster heterostructure remained unchanged compared to the pristine catalyst (Fig. S11 in the ESM), demonstrating outstanding electrochemical and structural stability under alkaline conditions. The long-term stability of the $N@Mo_2C/V_2O_3$ electrode under high-current density conditions was further evaluated through chronoamperometry (Fig. 3(f)). Remarkably, the catalyst maintained exceptional stabile operation at 110 mA·cm^{-2} with negligible current density decay over 400 h of continuous operation. These results confirm the outstanding durability of $N@Mo_2C/V_2O_3$ under high-current conditions in alkaline media, which is crucial for practical applications. Comparative analysis with previously reported alkaline-stable molybdenum-based HER catalysts (Fig. 3(g) and Table S4 in the ESM) reveals that $N@Mo_2C/V_2O_3$ exhibits superior performance, positioning it as a leading candidate within this material class with significant potential for commercial implementation.

To assess the HER selectivity of the $N@Mo_2C/V_2O_3$ cluster heterostructure, its Faradaic efficiency was measured (Fig. 4(a)). The calculated Faradaic efficiency approaches 100%, confirming

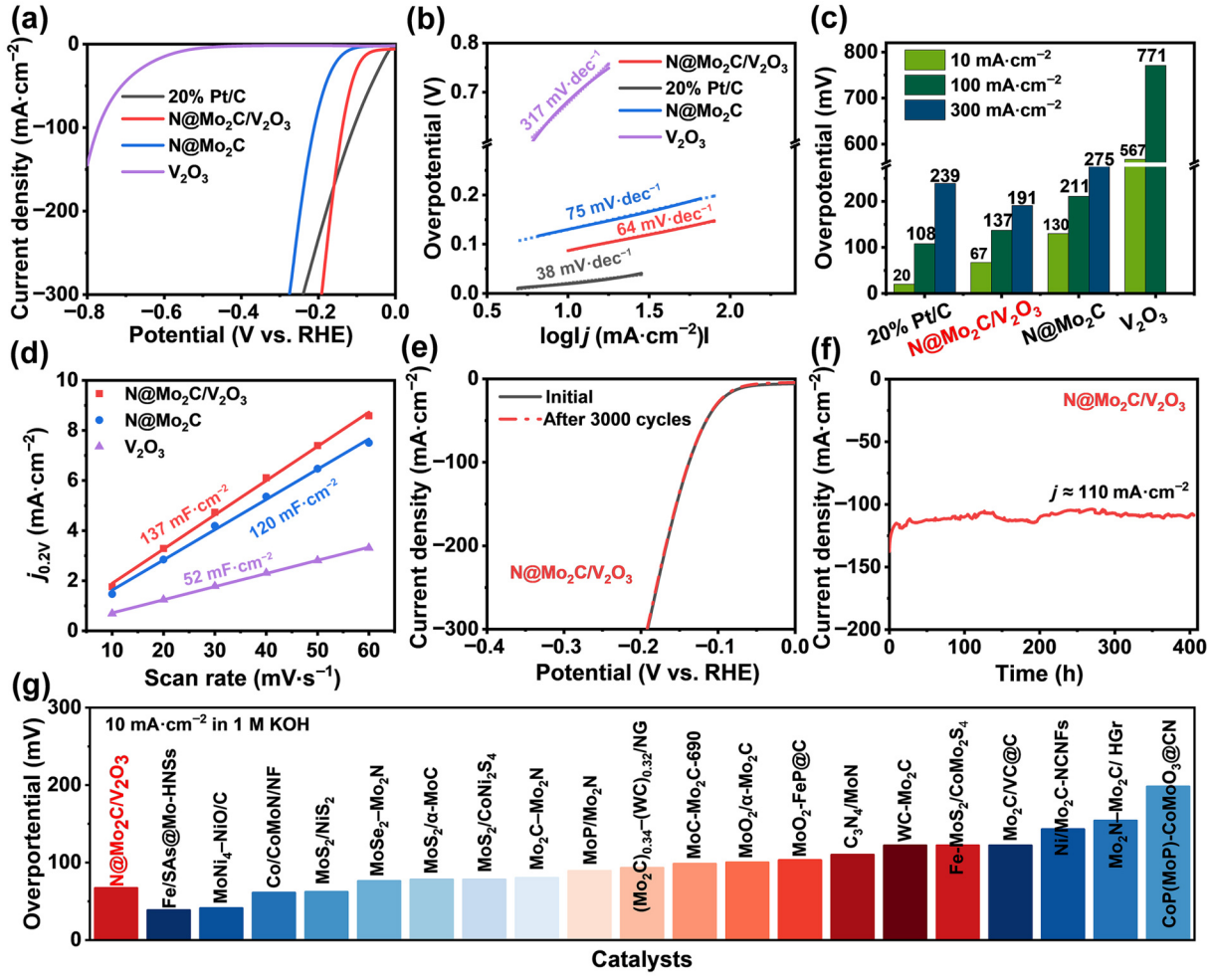

Figure 3 Electrocatalytic activity of the as-prepared materials for the HER in alkaline medium (1.0 M KOH). (a) *iR*-corrected polarization curves and (b) corresponding Tafel plots of the materials: $N@Mo_2C/V_2O_3$, $N@Mo_2C$, V_2O_3, and commercial 20 wt.% Pt/C. (c) Overpotentials at 10, 100, and 300 mA·cm^{-2}. (d) The C_{dl} of different catalysts. (e) LSV curves of the $N@Mo_2C/V_2O_3$ recorded before and after 1000 CV cycles of the HER. (f) Chronoamperometric curve of the $N@Mo_2C/V_2O_3$ at a constant potential of −0.14 V vs. RHE for 400 h. (g) Comparison of HER performances in 1.0 M KOH for $N@Mo_2C/V_2O_3$ with other reported catalysts.

near-perfect electrochemical selectivity for the HER. Additionally, a solar-driven water electrolysis device was constructed, directly powered by solar panels, as shown in Fig. 4(b) and Fig. S12 in the ESM. Even under continuous fluctuations in solar irradiance, $N@Mo_2C/V_2O_3$ remains stable in performing HER through water electrolysis (Fig. 4(c) and Table S5 in the ESM). The system achieved a hydrogen production rate of ~ 43 mL within 10 min, highlighting its potential for renewable energy applications. Based on the measured 100% Faraday efficiency, this corresponds to an effective current density of ~ 617 mA·cm^{-2} utilized by the catalytic electrode for hydrogen production. These findings demonstrate that the $N@Mo_2C/V_2O_3$ cluster heterostructure is a promising candidate for renewable hydrogen production in photo-electrochemical water-splitting systems.

To evaluate the commercial potential of $N@Mo_2C/V_2O_3$ cluster heterostructure for water electrolysis, large-area, self-supported $N@Mo_2C/V_2O_3$ electrodes were fabricated and employed as cathodes in AWE cells. Cell performance was evaluated with commercial Raney nickel or literature-reported NiFe-LDH catalysts serving as the anode. All electrochemical measurements were performed in a 30% KOH electrolyte at 60 °C under atmospheric pressure, without *iR* compensation. As shown in Fig. S13 in the ESM, when coupled with a commercial Raney nickel anode, the $N@Mo_2C/V_2O_3$ cathode achieved a current density of 500 mA·cm^{-2} at an applied voltage of 2.0 V. Although slightly less efficient than Pt/C at lower current densities (< 200 mA·cm^{-2}), the $N@Mo_2C/V_2O_3$||Zirfon||Raney nickel system exhibited a distinct advantage at higher current densities (> 200 mA·cm^{-2}), requiring a significantly lower operating voltage. The replacement of the conventional anode with a NiFe-LDH anode (Fig. 4(d)) notably improved overall performance of the $N@Mo_2C/V_2O_3$||Zirfon||NiFe-LDH electrolysis cell. Specifically, the cell voltage required to achieve 500 and 1000 mA·cm^{-2} decreased to 1.94 and 2.35 V, respectively, markedly lower than the 2.04 and 2.54 V needed for a Pt/C-based cell to reach the same high current densities. Under alkaline electrolyzer conditions, our catalyst exhibits moderate performance compared with previously reported catalysts (Table S6 in the ESM). Figure 4(f) shows the disassembled electrolysis cell, showing the sequence of components: anode shell, anode plate, anode current collector, anode catalyst, flow channel and reaction chamber (with commercial Zirfon separator), cathode catalyst, cathode current collector, cathode plate, and cathode shell. To ensure accuracy in evaluation, all assembly tests were repeated thrice, and the results were averaged. Furthermore, the performance of the AWE was further investigated at varying temperatures, demonstrating a positive correlation between

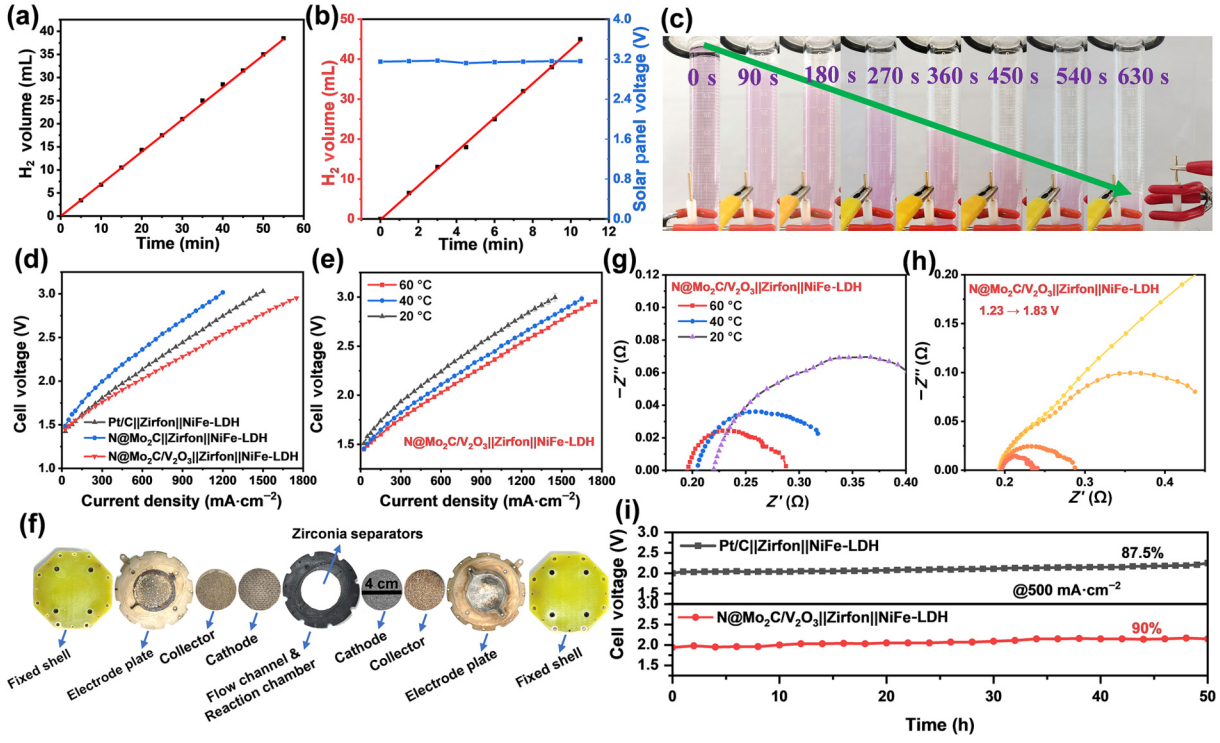

Figure 4 (a) Faraday efficiency test of $N@Mo_2C/V_2O_3$ at 100 mA·cm^{-2}, the dots in the figure represent tested data and the red line represents the theoretical value. (b) Solar panel coupled electrolysis of water for hydrogen production test. (c) Schematic of hydrogen collection by drainage method. (d) Performance of Pt/C||Zirfon||NiFe-LDH, $N@Mo_2C/C$||Zirfon||NiFe-LDH, and $N@Mo_2C/V_2O_3$||Zirfon||NiFe-LDH electrolytic cell. (e) Performance of $N@Mo_2C/V_2O_3$||Zirfon||NiFe-LDH electrolytic cell at different temperatures. (f) The sequence of components after disassembling the electrolysis cell. EIS of the $N@Mo_2C/V_2O_3$||Zirfon||NiFe-LDH electrolytic cell (g) at various temperatures and (h) under different voltages (1.23, 1.43, 1.63, and 1.83 V). (i) Curves of cell voltage variation with respect to time of Pt/C||Zirfon||NiFe-LDH and $N@Mo_2C/V_2O_3$||Zirfon||NiFe-LDH at 500 mA·cm^{-2} and 60 °C in 30 wt. % KOH.

operating temperature and electrolyzer efficiency (Fig. 4(e)).

To elucidate the origin of the performance enhancement, EIS measurements were performed on the $N@Mo_2C/V_2O_3$||Zirfon||NiFe-LDH electrolysis cell at various temperatures (Fig. 4(g)). The results revealed optimal charge transfer kinetics and reaction rates at 60 °C. Additional EIS measurements at different potentials showed consistent electrochemical kinetics throughout the water-splitting process, with further improvements in charge transfer kinetics at elevated potentials (Fig. 4(h)). This study also found that, compared to a conventional three-electrode system, the compact architecture of the electrolysis cell reduces ohmic resistance, enhancing electrolysis performance and efficiency. Finally, the long-term stability of the AWE was evaluated at an industrial current density of 500 mA·cm^{-2} (Fig. 4(i)). The Pt/C||Zirfon||NiFe-LDH configuration demonstrated moderate stability, with the cell potential rising to 2.25 V after 50 h of continuous operation, corresponding to 87.5% retention of the initial performance. By contrast, the $N@Mo_2C/V_2O_3$-based electrolyzer showed superior stability, maintaining 90% of its initial performance under identical conditions. The enhanced stability of $N@Mo_2C/V_2O_3$ can be attributed to its integrated, self-supported electrode architecture, which eliminates the need for polymeric binders that typically obstruct active sites and impede mass and electron transfer. Furthermore, the *in situ* growth of the catalyst on a conductive substrate provides robust interfacial adhesion, effectively mitigating material detachment during prolonged operation. These combined structural advantages underscore the strong potential of $N@Mo_2C/V_2O_3$ for industrial-scale hydrogen production [5].

3.4 Interpretation of the structure–activity relationship

A proportional mixture of Mo6-NAr and V10 was prepared to explore the advantages of dual-component heterojunctions. The mixture was subsequently grown and loaded onto CFP and then pyrolyzed in a H_2/Ar atmosphere at 650 °C for 3 h. As shown in the XRD pattern (Fig. S14(a) in the ESM), the resulting product consists of two distinct phases, $N@Mo_2C$ and V_2O_3, denoted as $N@Mo_2C+V_2O_3$, which can also be obtained through simple physical mixing and pyrolysis. However, the XRD diffraction peaks of the physically mixed sample are more intense compared to the $N@Mo_2C/V_2O_3$ cluster heterostructure, suggesting a larger grain size for the $N@Mo_2C$ nanoparticles. This is likely attributed to the severe aggregation of nanoparticles during sintering. The HER performance evaluation of the two catalysts demonstrated that the $N@Mo_2C/V_2O_3$ cluster heterostructure, synthesized from the well-designed Mo3V4-6NAr precursor, exhibited significantly enhanced catalytic activity than the physically mixed $N@Mo_2C+V_2O_3$ (Fig. S14(b) in the ESM). This superior performance can be attributed to the abundant heterointerfaces in $N@Mo_2C/V_2O_3$, which provide numerous active sites, highlighting the critical role of precursor molecular design in optimizing catalytic properties. Furthermore, the physically mixed samples displayed inferior electrochemical stability, with notable performance degradation after 3,000 CV cycles (Fig. S15(a) in the ESM). XRD patterns (Fig. S15(b) in the ESM) revealed a significant decrease in peak intensity corresponding to $N@Mo_2C$ in the $N@Mo_2C+V_2O_3$ composite after the HER test, suggesting potential structural degradation during the catalytic process. SEM characterization (Fig. S16 in the ESM)

further confirmed that the N@Mo_2C+V_2O_3 nanosheets underwent size reduction and exfoliation following the HER, confirming the poor mechanical stability of catalysts prepared via simple physical mixing.

Furthermore, we conducted a comprehensive analysis of the hydrophilicity, dynamic behavior of hydrogen bubble growth and desorption on the electrode surface, and electrical conductivity of the N@Mo_2C/V_2O_3 cluster heterostructure to investigate its outstanding performance at high current densities. Under alkaline conditions, superior hydrophilicity facilitates the adsorption of water molecules on catalytic surfaces, thereby promoting water dissociation. Water contact angle measurements (Fig. 5(a) and Fig. S17 in the ESM) demonstrated that pristine CFP (127.1°) is hydrophobic, whereas N@Mo_2C (97.4°) shows only moderate hydrophilicity. By contrast, both V_2O_3 (19.7°) and N@Mo_2C/V_2O_3 (18.9°) display significantly enhanced hydrophilicity, confirming that the introduction of V_2O_3 substantially enhances interfacial hydrophilicity. During hydrogen evolution, the size and detachment behavior of hydrogen bubbles provide macroscopic insight into the gas–liquid–solid interfacial properties of the catalyst surface. As shown in Fig. 5(b) and Movie S1 in the ESM, at a current density of 200 mA·cm^{-2}, hydrogen bubbles formed on V_2O_3 and N@Mo_2C/V_2O_3 are noticeably smaller and detach more readily than those observed on Pt/C and N@Mo_2C. This behavior suggests that N@Mo_2C/V_2O_3 exhibits more faster bubble detachment and more efficient gas release compared to pristine V_2O_3 and N@Mo_2C, thereby helping to maintain the exposure of active sites during prolonged hydrogen evolution. Resistivity measurements (Fig. 5(c) and Fig. S18 in the ESM) further revealed that V_2O_3, N@Mo_2C, and N@Mo_2C/V_2O_3 exhibit resistivities of 1, 0.02575, and 0.0407 Ω·cm, respectively, confirming that the N@Mo_2C/V_2O_3 heterojunction retains the high intrinsic electrical conductivity of N@Mo_2C. Collectively, these findings demonstrate that in the N@Mo_2C/V_2O_3 cluster heterostructure, N@Mo_2C serves as the primary active site with superior charge transfer capability, while V_2O_3 synergistically enhances hydrophilicity and hydrogen desorption kinetics. This dual functionality underpins the exceptional HER performance of the N@Mo_2C/V_2O_3 cluster heterostructure at high current densities.

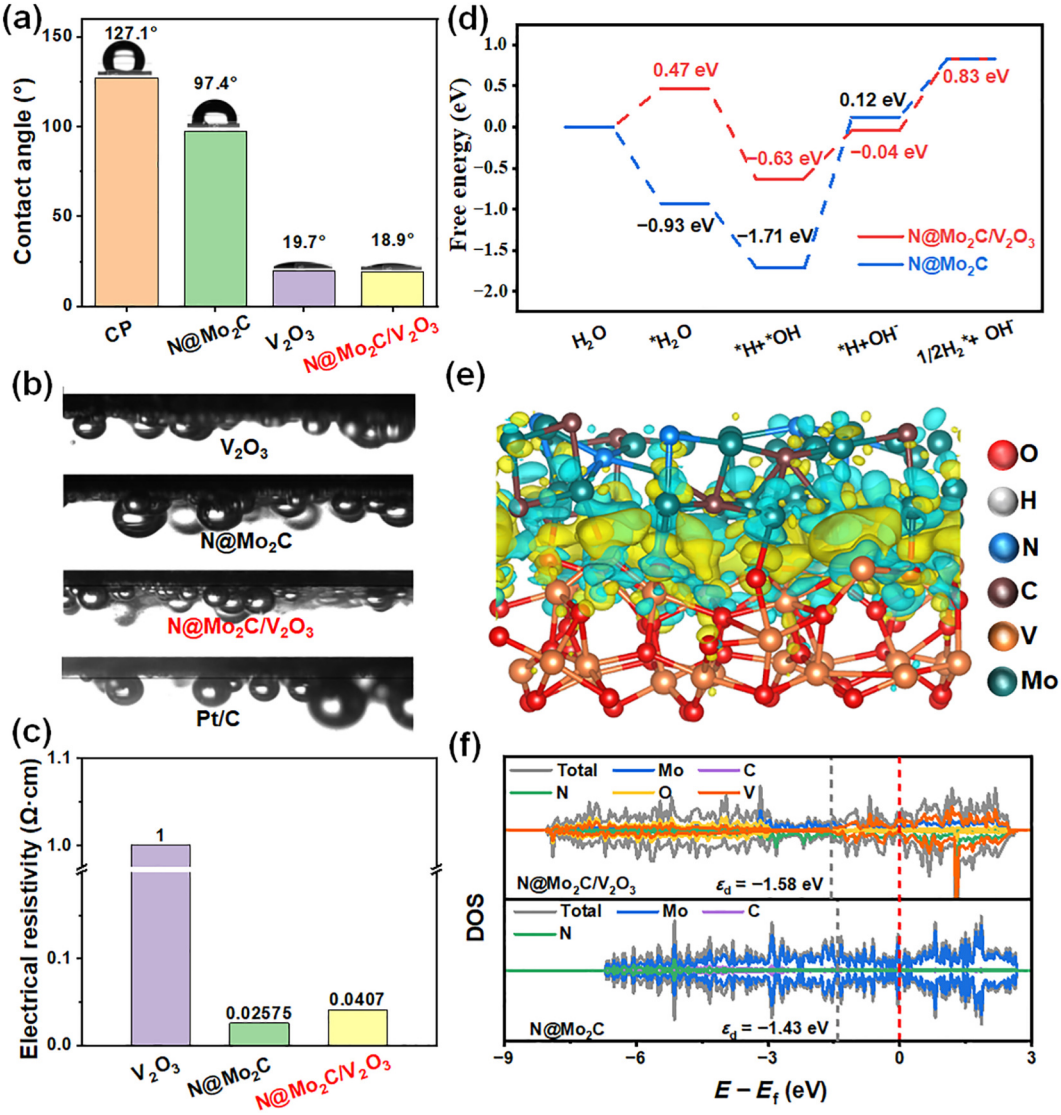

Figure 5 (a) Water contact angle. (b) *In situ* electron micrographs of the desorption of hydrogen. (c) Electrical resistivity of N@Mo_2C, V_2O_3, and N@Mo_2C/V_2O_3. (d) Reaction energy profiles of the complete alkaline HER reaction on the N@Mo_2C/V_2O_3 and N@Mo_2C system models. (e) Differential charge density diagram of N@Mo_2C/V_2O_3. (f) DOS spectra of Mo 4*d* for N@Mo_2C/V_2O_3 and N@Mo_2C.

To elucidate the mechanism underlying the enhanced alkaline HER activity, density functional theory (DFT) calculations were conducted on the N@Mo_2C/V_2O_3 cluster heterostructure. The structural model was constructed based on XRD and HRTEM results, featuring an interfacial configuration where N@Mo_2C(121) interfaces with V_2O_3(110) planes to form a crystalline heterojunction, as shown in Fig. S19 in the ESM. In alkaline media, the HER proceeds through sequential water adsorption, H_2O dissociation (Volmer step), OH^- desorption, and H_2 formation/desorption (Heyrovsky step) [60]. Our experimental results confirm that the overall reaction follows the Volmer–Heyrovsky pathway. A comparative investigation of the reaction pathways on N@Mo_2C/V_2O_3 and its single-component counterpart, N@Mo_2C, is shown in Figs. S20 and S21 in the ESM. As illustrated in Fig. 5(d), N@Mo_2C exhibits a relatively low water adsorption energy of −0.93 eV. However, the OH^- desorption step constitutes the rate-limiting step for N@Mo_2C, with a considerable energy barrier of 1.83 eV that severely restricts HER kinetics [8]. By contrast, while the water adsorption energy for the N@Mo_2C/V_2O_3 cluster heterostructure is slightly higher (0.43 eV), the interfacial interaction significantly facilitates the water dissociation and reduces the OH^- desorption energy barrier to 0.59 eV, which is much lower than that of N@Mo_2C. This considerable reduction in the OH^- desorption barrier greatly improves the overall reaction rate. Moreover, the energy barrier of the rate-determining step for N@Mo_2C/V_2O_3 is 0.87 eV, much lower than that of N@Mo_2C (1.83 eV), indicating that the optimized N@Mo_2C/V_2O_3 cluster heterostructure can effectively promote HER kinetics and leads to superior catalytic performance in alkaline media. The overall smoothness of the reaction pathway, with no kinetically prohibitive steps, ensures efficient reaction progress with minimal resistance, thus contributing to the excellent HER activity of N@Mo_2C/V_2O_3.

To further explore the impact of the electronic structure on the enhanced alkaline HER activity of N@Mo_2C/V_2O_3, differential charge density and density of states (DOS) analyses were performed [61, 62]. The charge density difference analysis (Fig. 5(e)) reveals distinct regions of electron accumulation (yellow) and depletion (cyan), demonstrating an inhomogeneous charge distribution at the N@Mo_2C–V_2O_3 interface. Notably, significant electron transfer occurs from N@Mo_2C to interfacial V_2O_3, creating a polarized charge distribution within the V–O–Mo interfacial system. Further, DOS analysis reveals continuous states at the Fermi level for both N@Mo_2C/V_2O_3 and N@Mo_2C (Fig. 5(f)), confirming their metallic character and high electronic conductivity [33]. The d-band center (ε_d) calculations demonstrate that Mo sites in N@Mo_2C/V_2O_3 exhibit a lower ε_d value (−1.58 eV) compared to pristine N@Mo_2C (−1.43 eV), representing a 0.15 eV downward shift relative to the Fermi level. This negative ε_d shift correlates with weakened hydrogen adsorption energy, which simultaneously promotes H_2 desorption and enhances the HER kinetics of N@Mo_2C/V_2O_3 [60, 62]. Consequently, the superior HER activity of the N@Mo_2C/V_2O_3 heterojunction arises from three key synergistic effects: (i) thermodynamically favorable OH^- desorption, which substantially lowers the energy barrier of the rate-determining step; (ii) moderated hydrogen adsorption free energy, which facilitates hydrogen release at the catalyst surface and is consistent with the experimentally observed formation of small, readily detachable hydrogen bubbles; (iii) enhanced electronic conductivity originating from the polarized V–O–Mo interfacial structure. Collectively, these factors enable efficient interfacial charge transport and smooth reaction pathways, thereby endowing N@Mo_2C/V_2O_3 with excellent catalytic performance in alkaline media.

4 Conclusion

Herein, we successfully synthesized a POM molecule precursor (Mo3V4-6NAr) with well-defined Mo–O–V and Mo–N bonds and subsequently constructed ultrafine N@Mo_2C/V_2O_3 cluster heterostructures via high-temperature pyrolysis. The superior HER performance of the optimized N@Mo_2C/V_2O_3 cluster heterostructure originates from electronically tuned interfacial structures, including interfacial charge redistribution (as evidenced by the positive shift of Mo 3d and the negative shift of V 2p in XPS) and the downshift of the Mo *d*-band center ($\Delta\varepsilon_d \approx -0.15$ eV) revealed by DFT calculations. These electronic modifications optimize hydrogen adsorption strength of Mo active sites, accelerate electron transfer across the interface of the N@Mo_2C/V_2O_3 cluster heterostructures, and enhance overall HER kinetics. As a result, the optimized catalyst achieves a current density of 300 mA·cm^{-2} at an overpotential of 191 mV and maintains stable operation for more than 400 h. In an AWE, it delivers 500 mA·cm^{-2} at 1.94 V, outperforming commercial 20 wt.% Pt/C. This study provides new insights into the rational design of high-performance, cost-effective cluster heterostructure catalysts and elucidates the synergistic roles of catalytic and co-catalytic active sites in regulating interfacial electron transfer and reaction pathways at the atomic level. Future research will focus on *in situ* spectroscopic monitoring of interfacial electronic states and precise modulation of coordination environments to further refine d-band tuning and hydrogen adsorption thermodynamics.

Electronic Supplementary Material: Supplementary material (including the preparation methods of the catalysts, the FT-IR, SEM, TEM, BET, Raman and XRD of the prepared samples, the TGA, XPS, ICP, the electrochemical data, and the structural model of the catalysts) is available in the online version of this article at https://doi.org/10.26599/POM.2026.9140110.

Data availability

All data needed to support the conclusions in the paper are presented in the manuscript and the Electronic Supplementary Material. Additional data related to this paper may be requested from the corresponding author upon request.

Acknowledgements

This work was financially supported by the National Natural Science Foundation of China (Nos. 22171287 and 52303274), Taishan Scholar Project of Shandong Province (No. tsqn202103046), Natural Science Foundation of Shandong Province (Nos. ZR2024QB076 and ZR2022QE175), Young Innovative Science and Technology Support Program for Universities of Shandong Province (Nos. 2021KJ014 and 2023KJ280), and Fundamental Research Funds for the Central Universities (No. 24CX07007A).

Declaration of competing interest

The authors have no competing interests to declare that are relevant to the content of this article.

Author contribution statement

L. L. C: Data curation, visualization, writing manuscript. Y. C. H: Conceptualization, supervision, project administration, funding acquisition. H. T. L: Experimental design, visualization, methodology. R. L. G: Visualization, supervision. H. T: Investigation. J. W. C: Validation. Y. F. W: Investigation. M. H. L: funding acquisition, supervision. C. D. W: Supervision, resources. All the authors have approved the final manuscript.

Use of AI statement

None.

References

[1] Zhang, J. H.; Fu, X. B.; Kwon, S.; Chen, K. F.; Liu, X. Z.; Yang, J.; Sun, H. R.; Wang, Y. C.; Uchiyama, T.; Uchimoto, Y. et al. Tantalum-stabilized ruthenium oxide electrocatalysts for industrial water electrolysis. *Science*. **2025**, *387*, 48–55.

[2] Shi, Z. Y.; Zhang, X.; Lin, X. Q.; Liu, G. G.; Ling, C. Y.; Xi, S. B.; Chen, B.; Ge, Y. Y.; Tan, C. L.; Lai, Z. C. et al. Phase-dependent growth of Pt on MoS_2 for highly efficient H_2 evolution. *Nature*. **2023**, *621*, 300–305.

[3] Gao, X. Q.; Chen, Y. T.; Wang, Y. J.; Zhao, L. Y.; Zhao, X. Y.; Du, J.; Wu, H. X.; Chen, A. B. Next-generation green hydrogen: Progress and perspective from electricity, catalyst to electrolyte in electrocatalytic water splitting. *Nano-Micro Lett.* **2024**, *16*, 237.

[4] Fu, H. C.; Chen, X. H.; Yang, B.; Luo, Y. H.; Li, T.; Wang, X. H.; Zhang, Q.; Li, X. L.; Li, N. B.; Luo, H. Q. Unveiling the *in-situ* hydrogen intercalation in MO_2CO_x for promoting the alkaline hydrogen evolution reaction. *Appl. Catal. B: Environ.* **2023**, *332*, 122739.

[5] Xiong, H.; Du, C. F.; Ma, Z. L.; Zhi, R. C.; Hao, S. S.; Zhao, X. Y.; Liu, Z.; Xu, F.; Wang, H. Q. Rational design of multiple heterostructures with synergistic effect for efficient and stable hydrogen evolution toward industrial alkaline water splitting. *Adv. Funct. Mater.* **2024**, *34*, 2402298.

[6] Sun, H. N.; Xu, X. M.; Kim, H.; Jung, W.; Zhou, W.; Shao, Z. P. Electrochemical water splitting: Bridging the gaps between fundamental research and industrial applications. *Energy Environ. Mater.* **2023**, *6*, e12441.

[7] Guo, L.; Xie, J.; Chen, S. Y.; He, Z. X.; Liu, Y. Z.; Shi, C. X.; Gao, R. J.; Pan, L.; Huang, Z. F.; Zhang, X. W. et al. Self-supported crystalline-amorphous composites of metal phosphate and NiS for high-performance water electrolysis under industrial conditions. *Appl. Catal. B: Environ.* **2024**, *340*, 123252.

[8] Liu, W.; Wang, X. T.; Wang, F.; Du, K. F.; Zhang, Z. F.; Guo, Y. Z.; Yin, H. Y.; Wang, D. H. A durable and pH-universal self-standing MoC-Mo_2C heterojunction electrode for efficient hydrogen evolution reaction. *Nat. Commun.* **2021**, *12*, 6776.

[9] He, D. Y.; Li, T. Y.; Jiang, L. Z.; Wang, F.; Xing, Z. H.; Wang, N.; Jia, Z. Y.; Yang, G. Y. Polyoxometalate as the assembly material to self-assembled $Ni(OH)_2$ nanosheets with electrocatalytic performance. *Nano Res.* **2024**, *17*, 7061–7067.

[10] Xie, J. Y.; Wang, F. L.; Zhou, Y. N.; Dong, Y. W.; Chai, Y. M.; Dong, B. Internal polarization field induced hydroxyl spillover effect for industrial water splitting electrolyzers. *Nano-Micro Lett.* **2024**, *16*, 39.

[11] Li, C. Y.; Wang, Z. J.; Liu, M. D.; Wang, E. Z.; Wang, B. L.; Xu, L. L.; Jiang, K. L.; Fan, S. S.; Sun, Y. H.; Li, J. et al. Ultrafast self-heating synthesis of robust heterogeneous nanocarbides for high current density hydrogen evolution reaction. *Nat. Commun.* **2022**, *13*, 3338.

[12] Yang, C. X.; Cai, Z. W.; Liang, J.; Dong, K.; Li, Z. X.; Sun, H.; Sun, S. J.; Zheng, D. D.; Zhang, H.; Luo, Y. S. et al. Surface-derived phosphate layer on NiFe-layered double hydroxide realizes stable seawater oxidation at the current density of 1 $A \cdot cm^{-2}$. *Nano Res.* **2024**, *17*, 5786–5794.

[13] Shang, Z. T.; Li, T. M.; Hu, B. Q.; Liu, M.; Lu, W. T.; Yu, F.; Zheng, Y. Two-dimensional bimetallic selenium-containing metal-organic frameworks and their calcinated derivatives as electrocatalysts for overall water splitting. *Front. Energy*. **2024**, *18*, 378–389.

[14] Wu, H. B.; Xia, B. Y.; Yu, L.; Yu, X. Y.; Lou, X. W. Porous molybdenum carbide nano-octahedrons synthesized via confined carburization in metal-organic frameworks for efficient hydrogen production. *Nat. Commun.* **2015**, *6*, 6512.

[15] Huang, Y. C.; Hu, J.; Xu, H. X.; Bian, W.; Ge, J. X.; Zang, D. J.; Cheng, D. J.; Lv, Y. K.; Zhang, C.; Gu, J. et al. Fine tuning electronic structure of catalysts through atomic engineering for enhanced hydrogen evolution. *Adv. Energy Mater.* **2018**, *8*, 1800789.

[16] Wan, J.; Liu, Q. P.; Wang, T. T.; Yuan, H. M.; Zhang, P.; Gu, X. Theoretical investigation of platinum-like catalysts of molybdenum carbides for hydrogen evolution reaction. *Solid State Commun*. **2018**, *284–286*, 25–30.

[17] Li, Y. F.; Wan, X. Y.; Chen, Z. G.; Ding, D.; Li, H.; Zhang, N.; Liu, D.; Cui, Y. Activity enhancement of molybdenum carbide in alkaline hydrogen evolution reaction through oxidation-gradient modulation. *ACS Catal.* **2024**, *14*, 16712–16722.

[18] Huang, Y. C.; Ge, J. X.; Hu, J.; Zhang, J. W.; Hao, J.; Wei, Y. G. Nitrogen-doped porous molybdenum carbide and phosphide hybrids on a carbon matrix as highly effective electrocatalysts for the hydrogen evolution reaction. *Adv. Energy Mater.* **2018**, *8*, 1701601.

[19] Chen, L. L.; Huang, Y. C.; Ding, Y. P.; Yu, P.; Huang, F.; Zhou, W. B.; Wang, L. M.; Jiang, Y. Y.; Li, H. T.; Cai, H. Q. et al. Interfacial engineering of atomic platinum-doped molybdenum carbide quantum dots for high-rate and stable hydrogen evolution reaction in proton exchange membrane water electrolysis. *Nano Res.* **2023**, *16*, 12186–12195.

[20] Zhou, M.; Jiang, X. L.; Kong, W. J.; Li, H. F.; Lu, F.; Zhou, X.; Zhang, Y. G. Synergistic effect of dual-doped carbon on Mo_2C nanocrystals facilitates alkaline hydrogen evolution. *Nano-Micro Lett.* **2023**, *15*, 166.

[21] Hou, L. Q.; Li, C.; Jang, H.; Kim, M. G.; Jiang, J. Z.; Cho, J.; Liu, S. G.; Liu, X. E. Rationally designed Mo/Ru-based multi-site heterogeneous electrocatalyst for accelerated alkaline hydrogen evolution reaction. *Adv. Mater.* **2024**, *36*, 2410039.

[22] Dinh, C. T.; Jain, A.; de Arquer, F. P. G.; De Luna, P.; Li, J.; Wang, N.; Zheng, X. L.; Cai, J.; Gregory, B. Z.; Voznyy, O. et al. Multi-site electrocatalysts for hydrogen evolution in neutral media by destabilization of water molecules. *Nat. Energy*. **2018**, *4*, 107–114.

[23] Fu, H. Q.; Zhou, M.; Liu, P. F.; Liu, P. R.; Yin, H. J.; Sun, K. Z.; Yang, H. G.; Al-Mamun, M.; Hu, P. J.; Wang, H. F.; et al. Hydrogen spillover-bridged Volmer/Tafel processes enabling ampere-level current density alkaline hydrogen evolution reaction under low overpotential. *J. Am. Chem. Soc.* **2022**, *144*, 6028–6039.

[24] Zhang, W. J.; Yang, L.; Li, Z.; Nie, G. Z.; Cao, X. J.; Fang, Z. Z.; Wang, X. J.; Ramakrishna, S.; Long, Y. Z.; Jiao, L. F. Regulating hydrogen/oxygen species adsorption via built-in electric field -driven electron transfer behavior at the heterointerface for efficient water splitting. *Angew. Chem., Int. Ed.* **2024**, *63*, e202400888.

[25] Duan, Y.; Zhang, X. L.; Gao, F. Y.; Kong, Y.; Duan, Y.; Yang, X. T.; Yu, X. X.; Wang, Y. R.; Qin, S.; Chen, Z. et al. Interfacial engineering of Ni/V_2O_3 heterostructure catalyst for boosting hydrogen oxidation reaction in alkaline electrolytes. *Angew. Chem., Int. Ed.* **2023**, *62*, e202217275.

[26] Hu, H. S.; Zhang, Z. R.; Liu, L. J.; Che, X. L.; Wang, J. C.; Zhu, Y.; Attfield, J. P.; Yang, M. H. Efficient and durable seawater electrolysis

with a V_2O_3-protected catalyst. *Sci. Adv.* **2024**, *10*, eadn7012.
[27] Zhao, Z. C.; Wei, J. Y.; Lang, Z. L.; Chi, M. Z.; Liu, X. Y.; Yang, J. X.; Yang, G. Y.; Lv, H. J. A superatomic $\{Ag_8\}^{6+}$ cluster induced by asymmetric mixed-addendum polyoxometalate. *J. Am. Chem. Soc.* **2025**, *147*, 25107–25114.
[28] Chi, M. Z.; Wei, J. Y.; Zhao, Z. C.; Liu, X. Y.; Sun, W. T.; Feng, Y. Q.; Lv, H. J.; Yang, G.-Y. Structural isomerism of $\{Ag_{14}\}^{10+}$ nanocluster encapsulated by bowl-like polyoxometalates. *Angew. Chem., Int. Ed.* **2025**, *64*, e202424499.
[29] Feng, Y. Q.; Zhao, M. Y.; Yang, J. X.; Wang, Z. M.; Bai, P. H.; Liu, Y. K.; Lv, H. J.; Yang, G. Y. Wearing gigantic silver armor on transition-metal-containing polyoxometalates: Formation of supertetrahedral intercluster compounds. *Angew. Chem., Int. Ed.* **2025**, *64*, e202505511.
[30] Feng, Y. Q.; Fu, F. Y.; Zeng, L. L.; Zhao, M. Y.; Xin, X.; Liang, J. K.; Zhou, M.; Fang, X. K.; Lv, H. J.; Yang, G. Y. Atomically precise silver clusters stabilized by lacunary polyoxometalates with photocatalytic CO_2 reduction activity. *Angew. Chem., Int. Ed.* **2024**, *63*, e202317341.
[31] Horn, M. R.; Singh, A.; Alomari, S.; Goberna-Ferrón, S.; Benages-Vilau, R.; Chodankar, N.; Motta, N.; Ostrikov, K.; MacLeod, J.; Sonar, P. et al. Polyoxometalates (POMs): From electroactive clusters to energy materials. *Energy Environ. Sci.* **2021**, *14*, 1652–1700.
[32] Zeb, Z.; Huang, Y. C.; Chen, L. L.; Zhou, W. B.; Liao, M. H.; Jiang, Y. Y.; Li, H. T.; Wang, L. M.; Wang, L.; Wang, H. et al. Comprehensive overview of polyoxometalates for electrocatalytic hydrogen evolution reaction. *Coord. Chem. Rev.* **2023**, *482*, 215058.
[33] Huang, Y. C.; Zhou, W. B.; Kong, W. C.; Chen, L. L.; Lu, X. L.; Cai, H. Q.; Yuan, Y. R.; Zhao, L. M.; Jiang, Y. Y.; Li, H. T. et al. Atomically interfacial engineering on molybdenum nitride quantum dots decorated N-doped graphene for high-rate and stable alkaline hydrogen production. *Adv. Sci.* **2022**, *9*, 2204949.
[34] Huang, Y. C.; Sun, Y. H.; Zheng, X. L.; Aoki, T.; Pattengale, B.; Huang, J. E.; He, X.; Bian, W.; Younan, S.; Williams, N. et al. Atomically engineering activation sites onto metallic 1T-MoS_2 catalysts for enhanced electrochemical hydrogen evolution. *Nat. Commun.* **2019**, *10*, 982.
[35] Zhou, W. B.; Huang, Y. C.; Cai, H. Q.; Wang, T.; Li, H. T.; Zhang, C.; Zhao, L. M.; Chen, L. L.; Liao, M. H.; Tang, Z. Q. et al. A strongly coupled cluster heterostructure with Pt–N–Mo bonding for durable and efficient H_2 evolution in anion-exchange membrane water electrolyzers. *Nano-Micro Lett.* **2025**, *17*, 296.
[36] Zang, D. J.; Li, Q.; Dai, G. Y.; Zeng, M. Y.; Huang, Y. C.; Wei, Y. G. Interface engineering of Mo_8/Cu heterostructures toward highly selective electrochemical reduction of carbon dioxide into acetate. *Appl. Catal. B: Environ.* **2021**, *281*, 119426.
[37] Zang, D. J.; Wang, H. Q. Polyoxometalate-based nanostructures for electrocatalytic and photocatalytic CO_2 reduction. *Polyoxometalates* **2022**, *1*, 9140006.
[38] Jin, D. Y.; Qiao, F.; Zhou, Y.; Wang, J. F.; Cao, K. C.; Yang, J.; Zhao, J. K.; Zhou, L.; Li, H. T. Cu/Mo_2C synthesized through Anderson-type polyoxometalates modulate interfacial water structure to achieve hydrogen evolution at high current density. *Nano Res.* **2024**, *17*, 2546–2554.
[39] Huang, Y. C.; Zhang, J. W.; Ge, J. X.; Sui, C.; Hao, J.; Wei, Y. G. $[V_4Mo_3O_{14}(NAr)_3(\mu_2\text{-}NAr)_3]^{2-}$: The first polyarylimido-stabilized molybdovanadate cluster. *Chem. Commun*. **2017**, *53*, 2551–2554.
[40] Cai, Q. M.; Gao, R. L.; Wang, Y. F.; Xing, J. S.; Zhang, Q. Y.; Zhu, M. Z.; Qin, X. Y.; Liao, M. H.; Huang, Y. C. Ruthenium containing polyoxometalates: From synthesis, structures, properties to functional applications. *Polyoxometalates* **2025**, *4*, 9140083.
[41] Xu, L.; Xu, Y. P.; Xia, B.; Guo, B. R.; Kamal, K. M.; Likozar, B.; Li, X. M.; Dong, F. F.; Li, S. W.; Ma, Y. F. Surface single atom alloys for alkaline hydrogen evolution reaction. *Adv. Mater.* **2025**, *37*, 2502989.
[42] He, L. Q.; Zhang, W. B.; Mo, Q. J.; Huang, W. J.; Yang, L. C.; Gao, Q. S. Molybdenum carbide-oxide heterostructures: *In situ* surface reconfiguration toward efficient electrocatalytic hydrogen evolution. *Angew. Chem., Int. Ed.* **2020**, *59*, 3544–3548.
[43] Zhang, Y. Z.; Guo, P.; Guo, S. H.; Xin, X.; Wang, Y. J.; Huang, W. J.; Wang, M. H.; Yang, B. W.; Jorge Sobrido, A.; Ghasemi, J. B. et al. Gradient heating epitaxial growth gives well lattice-matched Mo_2C–Mo_2N heterointerfaces that boost both electrocatalytic hydrogen evolution and water vapor splitting. *Angew. Chem., Int. Ed.* **2022**, *61*, e202209703.
[44] Yan, H. J.; Xie, Y. L.; Jiao, Y. Q.; Wu, A. P.; Tian, C. G.; Zhang, X. M.; Wang, L.; Fu, H. G. Holey reduced graphene oxide coupled with an Mo_2N–Mo_2C heterojunction for efficient hydrogen evolution. *Adv. Mater.* **2018**, *30*, 1704156.
[45] Lu, P.; Huo, J. J.; Cui, M. J.; Dou, Y. H.; Li, W. X.; Liu, H. K.; Bai, Z. C.; Dou, S. X.; Ge, R. Y. Synergistic interface engineering of $Ni_{0.2}Mo_{0.8}N$/MoO_2 heterostructure catalysts for accelerated hydrogen evolution in alkaline water and seawater. *Adv. Funct. Mater.*, in press, DOI: 10.1002/adfm.202516798.
[46] Mai, T. D.; Do, H. H. Integrated strategies on cobalt phosphides-based electrocatalysts for efficient hydrogen evolution reaction. *Tungsten* **2024**, *6*, 488–503.
[47] Liu, H.; Shen, W.; Jin, H. Y.; Xu, J.; Xi, P. X.; Dong, J. C.; Zheng, Y.; Qiao, S. Z. High-performance alkaline seawater electrolysis with anomalous chloride promoted oxygen evolution reaction. *Angew. Chem., Int. Ed.* **2023**, *62*, e202311674.
[48] Chen, L. L.; Huang, Y. C.; Wang, J. J.; Liao, M. H.; Liu, Z. Y.; Liu, M. Q.; Cai, H. Q.; Wang, L.; Gao, L. D.; Hu, D. W. et al. Growth behavior and electronic regulation of Pt on various Mo-based supports for hydrogen evolution electrocatalysis. *Sci. China Chem.* **2025**, *68*, 1837–1846.
[49] Yang, Y.; Luo, M. C.; Xing, Y.; Wang, S. T.; Zhang, W. Y.; Lv, F.; Li, Y. J.; Zhang, Y. L.; Wang, W.; Guo, S. J. A universal strategy for intimately coupled carbon nanosheets/MoM nanocrystals (M = P, S, C, and O) hierarchical hollow nanospheres for hydrogen evolution catalysis and sodium-ion storage. *Adv. Mater.* **2018**, *30*, 1706085.
[50] Yang, G. C.; Jiao, Y. Q.; Yan, H. J.; Xie, Y.; Wu, A. P.; Dong, X.; Guo, D. Z.; Tian, C. G.; Fu, H. G. Interfacial engineering of MoO_2–FeP heterojunction for highly efficient hydrogen evolution coupled with biomass electrooxidation. *Adv. Mater.* **2020**, *32*, 2000455.
[51] Shi, X.; Wu, A. P.; Yan, H. J.; Zhang, L.; Tian, C. G.; Wang, L.; Fu, H. G. A "MOFs plus MOFs" strategy toward Co–Mo_2N tubes for efficient electrocatalytic overall water splitting. *J. Mater. Chem. A* **2018**, *6*, 20100–20109.
[52] Biesinger, M. C.; Lau, L. W. M.; Gerson, A. R.; Smart, R. S. C. Resolving surface chemical states in XPS analysis of first row transition metals, oxides and hydroxides: Sc, Ti, V, Cu and Zn. *Appl. Surf. Sci.* **2010**, *257*, 887–898.
[53] Zhang, Q.; Liu, B. Q.; Li, L.; Ji, Y.; Wang, C. G.; Zhang, L. Y.; Su, Z. M. Maximized schottky effect: The ultrafine V_2O_3/Ni heterojunctions repeatedly arranging on monolayer nanosheets for efficient and stable water-to-hydrogen conversion. *Small* **2021**, *17*, 2005769.
[54] Li, J. S.; Wang, Y.; Liu, C. H.; Li, S. L.; Wang, Y. G.; Dong, L. Z.; Dai, Z. H.; Li, Y. F.; Lan, Y. Q. Coupled molybdenum carbide and reduced graphene oxide electrocatalysts for efficient hydrogen evolution. *Nat. Commun.* **2016**, *7*, 11204.
[55] Zang, D. J.; Gao, X. J.; Li, L. Y.; Wei, Y. G.; Wang, H. Q. Confined interface engineering of self-supported Cu@N-doped graphene for electrocatalytic CO_2 reduction with enhanced selectivity towards ethanol. *Nano Res.* **2022**, *15*, 8872–8879.
[56] Yu, W. H.; Huang, H.; Qin, Y. N.; Zhang, D.; Zhang, Y. Y.; Liu, K.; Zhang, Y.; Lai, J. P.; Wang, L. The synergistic effect of pyrrolic-N and pyridinic-N with Pt under strong metal-support interaction to

achieve high-performance alkaline hydrogen evolution. *Adv. Energy Mater.* **2022**, *12*, 2200110.
[57] Li, Q. C.; Fu, X. W.; Li, H. D.; Xiao, Z. Y.; Xu, G. R.; Chen, D. H.; Li, C. X.; Jin, W.; Ma, T. Y.; Wu, Z. X. et al. Strong d-p orbital hybridization of Os–P via ultrafast microwave plasma assistance for anion exchange membrane electrolysis. *Adv. Funct. Mater.* **2024**, *34*, 2408517.
[58] Zhou, B. W.; Wang, J. P.; Guo, L. F.; Li, H. D.; Xiao, W. P.; Xu, G. R.; Chen, D. H.; Li, C. X.; Du, Y. M.; Ding, H. et al. Microwave-assisted PtRu alloying on defective tungsten oxide: A pathway to improved hydroxyl dynamics for highly-efficient hydrogen evolution reaction. *Adv. Energy Mater.* **2024**, *14*, 2402372.
[59] Chen, W.; Wu, B. B.; Wang, Y. Y.; Zhou, W.; Li, Y. Y.; Liu, T. Y.; Xie, C.; Xu, L. T.; Du, S. Q.; Song, M. L. et al. Deciphering the alternating synergy between interlayer Pt single-atom and NiFe layered double hydroxide for overall water splitting. *Energy Environ. Sci.* **2021**, *14*, 6428–6440.
[60] Wang, X. M.; Long, G. F.; Liu, B.; Li, Z. L.; Gao, W. S.; Zhang, P. F.; Zhang, H.; Zhou, X.; Duan, R. Z.; Hu, W. et al. Rationally modulating the functions of Ni_3SN_2–$NiSNO_X$ nanocomposite electrocatalysts towards enhanced hydrogen evolution reaction. *Angew. Chem., Int. Ed.* **2023**, *62*, e202301562.
[61] Wang, R. N.; Chen, Q.; Liu, X. Z.; Hu, Y. B.; Cao, L. X.; Dong, B. H. Synergistic effects of dual-doping with Ni and Ru in monolayer VS_2 nanosheet: Unleashing enhanced performance for acidic HER through defects and strain. *Small* **2024**, *20*, 2311217.
[62] Hou, L. Q.; Li, Z. J.; Jang, H.; Kim, M. G.; Cho, J.; Zhong, W. W.; Liu, S. G.; Liu, X. E. Partially interstitial silicon-implanted ruthenium as an efficient electrocatalyst for alkaline hydrogen evolution. *Angew. Chem., Int. Ed.* **2025**, *64*, e202423756.

Lulu Chen received her Ph.D. degree from China University of Petroleum (East China) in 2024. She is currently working as a lecturer at the School of Intelligent Manufacturing and Control Engineering, Shandong Institute of Petroleum and Chemical Technology. Her research interests focus on nanomaterials and electrochemical catalysis.

Yichao Huang received his Ph.D. degree from Tsinghua University in 2019. He is currently working as a professor at the School of Materials Science and Engineering, China University of Petroleum (East China). His research interests focus on developing polyoxometalate clusters for high-performance electrocatalysts in water splitting, fuel cell, electrochemical hydrogen compressor.

Haitao Li obtained a master's degree in Materials Science and Engineering from China University of Petroleum (East China) in 2024. His research mainly focuses on the synthesis and catalytic applications of polyoxometalates.

Ruili Gao is a Ph.D. candidate in Materials Science and Engineering at China University of Petroleum (East China). Her research mainly focuses on developing high-performing electrocatalysts for acidic oxygen evolution reaction (OER) in proton exchange membrane (PEM) water electrolysis.

Han Tang is a Ph.D. candidate in Materials Science and Engineering at the East China University of Petroleum. Her research mainly focuses on hydrodesulfurization.

Jiangwei Chen is a postgraduate student at China University of Petroleum (East China). Her main research focuses on bifunctional catalysts for HER/HOR.

Yanfei Wang is a postgraduate student at China University of Petroleum (East China). His main research focuses on ammonia synthesis and the oxygen evolution reaction (OER).

Meihong Liao received her Ph.D. degree from Beijing University of Chemical Technology in 2020. She is currently working as an associate professor at the Qingdao Binhai University. Her research focuses on the functional design of polymers and polyoxometalates for water electrolysis.

Chuande Wu is currently working as a professor at China University of Petroleum (East China). He focuses on the preparation and catalytic property research of biomimetic framework materials. Specifically, he employs simulated enzyme active centers as synthons to fabricate biomimetic framework materials, utilizes nanocages as microreactors and nanopores as transport channels, and achieves efficient enzyme-mimetic catalysis under mild conditions by regulating the catalytic microenvironment of the simulated enzymes.